

## Post-perihelion Coma Composition of the Interstellar Comet 3I/ATLAS from Optical Spectroscopy

RUINING ZHAO (赵瑞宁) <sup>1</sup>, XILIANG ZHANG (张西亮)<sup>2,3</sup>, BIN YANG (杨彬) <sup>4,5</sup>, XIANGYU FAN,<sup>2,3</sup> SHU WANG (王舒) <sup>1</sup>,  
YANG HUANG (黄样)<sup>3</sup> AND JIFENG LIU (刘继峰)<sup>1,3,6,7</sup>

<sup>1</sup>CAS Key Laboratory of Optical Astronomy, National Astronomical Observatories, Chinese Academy of Sciences, Beijing 100101, China

<sup>2</sup>Yunnan Observatories, Chinese Academy of Sciences (CAS), Kunming 650216, China

<sup>3</sup>School of Astronomy and Space Sciences, University of Chinese Academy of Sciences, Beijing 100049, China

<sup>4</sup>Instituto de Estudios Astrofísicos, Facultad de Ingeniería y Ciencias, Universidad Diego Portales, Santiago, Chile

<sup>5</sup>Planetary Science Institute, 1700 E Fort Lowell Rd STE 106, Tucson, AZ 85719, USA

<sup>6</sup>Institute for Frontiers in Astronomy and Astrophysics, Beijing Normal University, Beijing 102206, China

<sup>7</sup>New Cornerstone Science Laboratory, National Astronomical Observatories, Chinese Academy of Sciences, Beijing 100012, China

### ABSTRACT

We present multi-epoch optical spectroscopy of the interstellar comet 3I/ATLAS obtained from December 2025 to January 2026 (heliocentric distances 1.8 to 3.3 au). From these spectra, we derive post-perihelion production rates and/or mixing ratios for daughter molecules (CN, C<sub>3</sub>, C<sub>2</sub>, and CH) and gaseous metals (Fe I and Ni I). We also estimate a lower limit on the CO abundance based on the [O I]  $\lambda$ 6300 line. The resulting outgassing profiles reveal a pronounced perihelion asymmetry, with volatile production declining more gradually outbound than during the inbound phase. In addition, the coma becomes less depleted in C<sub>2</sub> following perihelion, and shows a substantial increase, relative to H<sub>2</sub>O, in the production rates of metals and potentially also CO. These trends may indicate the activation of subsurface material or compositional heterogeneity revealed by seasonal effects. The inferred high CO abundance further suggests possible decoupling of CO from H<sub>2</sub>O and CO<sub>2</sub>, similar to the behavior observed in solar system comets. The potential post-perihelion enhancement of both CO and metal production, if confirmed, would also be consistent with metal carbonyls contributing to the release of gaseous metals in cometary comae.

*Keywords:* Interstellar Objects (52) — Comets (280) — Comet Nuclei (2160) — Comae (271) — Comet Volatiles (2162) — Comet origins (2203) — Young stellar objects (1834) — Spectroscopy (1558)

### 1. INTRODUCTION

Interstellar objects (ISOs) are small bodies that formed in the protoplanetary disks of other stars and were later ejected into interstellar space (D. Jewitt & D. Z. Seligman 2023; A. Fitzsimmons et al. 2024). Their rare visits to the solar system provide a unique opportunity to sample the physical and chemical properties of distant planetary systems. Comparing these objects with solar system comets places our own system in a broader context and highlights the key factors that govern planet formation across diverse environments.

The first known ISO, 1I/‘Oumuamua, was discovered in 2017 (G. V. Williams et al. 2017; K. J. Meech et al. 2017). Although it exhibited a measurable non-gravitational acceleration likely caused by comet-like

outgassing (M. Micheli et al. 2018), no gas species were detected spectroscopically, leaving its composition largely unconstrained (Q.-Z. Ye et al. 2017; A. Fitzsimmons et al. 2018). By contrast, the second ISO, 2I/Borisov, was discovered in 2019 with a well-developed coma that allowed detailed compositional studies (G. Borisov et al. 2019). It was found to have a very high CO abundance relative to water compared with most solar system comets, placing it among the most CO-rich comets known (D. Bodewits et al. 2020; M. A. Cordiner et al. 2020). Moreover, its high linear polarization resembled that of C/1995 O1 (Hale-Bopp), suggesting a relatively pristine nature (S. Bagnulo et al. 2021). These properties underscore the physical and chemical distinctiveness of 2I/Borisov and highlight the potential of ISOs to probe the diversity of planetary formation environments.

Corresponding author: Ruining Zhao and Xiliang Zhang

The third ISO, 3I/ATLAS (hereafter 3I), was discovered in July 2025 and passed perihelion in late October of the same year (L. Denneau et al. 2025). Pre-perihelion observations indicated an extremely carbon-chain depleted composition (L. E. Salazar Manzano et al. 2025; M. Lazzarin et al. 2026), but with an unusually high CO<sub>2</sub> abundance relative to water (M. A. Cordiner et al. 2025; C. Lisse et al. 2026). Atomic nickel (Ni I) was first detected at a heliocentric distance of  $r_h = 3.78$  au, whereas atomic iron (Fe I) was identified only later at  $r_h = 2.64$  au, yielding an initially elevated Ni/Fe ratio that later approached typical values observed in solar system comets (R. Rahatgaonkar et al. 2025; W. B. Hoogendam et al. 2025a,b; D. Hutsemékers et al. 2026).

Following perihelion, the water production rate declined more gradually than during the inbound leg, producing pronounced perihelion asymmetry (H. Tan et al. 2026). At the same time, the C<sub>2</sub>/CN ratio became less depleted, and metal production rates increased significantly relative to their inbound values (W. B. Hoogendam et al. 2026; E. Jehin et al. 2025a,b). An enhanced CH<sub>4</sub> abundance was also reported, marking the first detection of CH<sub>4</sub> in an ISO (M. Belyakov et al. 2026). However, most previous measurements were obtained at isolated epochs, providing only limited constraints on how the coma composition evolves after perihelion.

Here we present multi-epoch optical spectroscopic observations of 3I obtained with 2-m class telescopes following perihelion, allowing us to directly trace the temporal evolution of the coma composition during the outbound phase. The observation and data reduction are described in Section 2. The reduced spectra are modeled and analyzed in Section 3. The results are discussed in Section 4 and summarized in Section 5.

## 2. OBSERVATION AND DATA REDUCTION

### 2.1. 2.16-meter telescope

We obtained four long-slit spectra of 3I in 2025 December with the Beijing Faint Object Spectrograph and Camera (BFOSC) mounted on the Xinglong 2.16-meter Telescope. The instrument is equipped with a 2K × 2K CCD featuring a pixel scale of 0''274 (Z. Fan et al. 2016). A 2''3 × 9''4 slit was used and fixed in the north-south direction. As the observations were conducted within ~1 hr of transit, this orientation remained nearly aligned

with the parallactic angle, thereby minimizing atmospheric dispersion. The G3 grism, covering 330–660 nm, was used, delivering a resolving power of  $R \sim 320$  when combined with the 2''3 slit. Bias frames, dome flats, and Fe-Ar arc lamp exposures were obtained each afternoon. During the night, 3I was observed together with a nearby solar analog and a flux standard for calibration. The solar analogs were selected from the LAMOST solar-type star catalog (J. Zhang et al. 2020) and have been verified to exhibit solar-like spectra. Slit-view images were obtained for each target prior to science exposures and were used in the reduction to estimate and correct for slit losses caused by seeing variations. A brief observing log is provided in Table 1, with the full version given in Appendix A.

The data were reduced with the ASTRO-PLPY<sup>8</sup> package following standard procedures for long-slit spectroscopy, with additional treatments described in Appendix A. One-dimensional spectra were extracted using a fixed aperture of 80 pixels (or 21''9).

### 2.2. 2.40-meter telescope

In addition to the BFOSC observations, we obtained eight long-slit spectra of 3I in 2025 December and 2026 January using the Yunnan Faint Object Spectrograph and Camera (YFOSC) mounted on the 2.4-meter Lijiang telescope. The instrument is equipped with a 2K × 4K CCD featuring a pixel scale of 0''283 (C.-J. Wang et al. 2019). Observations were carried out with the G3 grism and a 2''5 × 9''4 slit fixed in the north-south direction. This configuration yields a resolving power of  $R \sim 280$  over the wavelength range 320–930 nm. Dome flats were obtained either before or after each observing night. During each night, 3I was observed together with a nearby solar analog and a flux standard. Wavelength calibration was performed using a He-Ne arc lamp and further refined using observations of the planetary nebula NGC 2392. The observing log is also provided in Table 1, with the full version given in Appendix A.

The data reduction followed the same procedures adopted for the BFOSC spectra, with additional treatments described in Appendix A. One-dimensional spectra were extracted using a fixed aperture of 80 pixels (or 22''6).

<sup>8</sup> <https://github.com/RuiningZHAO/plpy>

**Table 1.** Observation log of 3I/ATLAS.

Date of 2025 (UT)	$\Delta^a$ (au)	$r_h^b$ (au)	$\dot{r}_h^c$ (km s <sup>-1</sup> )	Tel./Inst.	$\lambda^d$	Slit Width ( $''$ )	Exposure (s)	Airmass
Dec. 2	1.892	1.846	42.44	2.16-m/BFOSC	330–660	2.3	4×300	1.72–1.61
Dec. 20	1.799	2.333	50.43	...	...	...	3×300	1.22–1.21
Dec. 23	1.807	2.423	51.28	...	...	...	8×300	1.18–1.22
Dec. 26	1.823	2.509	52.00	...	...	...	8×300	1.19–1.26
Dec. 4	1.872	1.898	43.71	2.40-m/YFOSC	320–930	2.5	300	1.21
Dec. 6	1.855	1.947	44.78	...	...	...	4×300	1.78–1.60
Dec. 7	1.846	1.973	45.32	...	...	...	3×300	1.47–1.40
Dec. 17	1.798	2.246	49.48	...	...	...	2×300	1.45–1.41
Dec. 19	1.798	2.306	50.15	...	...	...	2×300	1.07
Dec. 28	1.840	2.570	52.45	...	...	...	300	1.13
Jan. 11 <sup>e</sup>	2.064	3.002	54.76	...	...	...	2×300	1.13–1.11
Jan. 20 <sup>e</sup>	2.311	3.293	55.75	...	...	...	600	1.27

<sup>a</sup>Geocentric distance.

<sup>b</sup>Heliocentric distance.

<sup>c</sup>Heliocentric radial velocity.

<sup>d</sup>Wavelength coverage.

<sup>e</sup>Date of 2026.

### 3. RESULTS AND ANALYSIS

The optical spectra of 3I exhibit gas emissions superimposed on a dust-scattered solar continuum. To isolate the gas component, we model the continuum by multiplying the spectrum of a solar analog by a low-order polynomial or a B-spline function and then subtract the best-fitting models from the observed spectra. As shown in Figure 1, the resulting pure emission spectra display rich gas emission features, including molecular bands of CN, C<sub>3</sub>, C<sub>2</sub>, and CH, atomic lines of FeI and NiI, and the [O I]  $\lambda\lambda 6300, 6364$  doublet. In the following subsections, we will derive the production rates and mixing ratios for the species related to these emission features and analyze their evolution compared to pre-perihelion measurements.

#### 3.1. CN, C<sub>3</sub>, C<sub>2</sub>, and CH

Our analysis begins with the carbon-bearing daughter molecules detected in the spectra. Production rates of these daughter molecules are derived using Haser model (L. Haser 1957), with an expansion velocity of  $v_{\text{exp}} = 0.85 \text{ km s}^{-1} \cdot (r_h/\text{au})^{-0.5}$ , and the  $g$ -factors and scale lengths from A. L. Cochran et al. (2012). The production rates of CN ( $Q_{\text{CN}}$ ) and the mixing ratios of other

species relative to CN ( $Q_X/Q_{\text{CN}}$ ) are listed in Table 2 on a logarithmic scale. Several measurements beyond  $r_h \sim 2.5$  au are unavailable due to low signal-to-noise ratios (SNRs).

Figure 2 illustrates the logarithmic  $Q_{\text{CN}}$  as a function of  $r_h$ , with pre-perihelion measurements from D. Hutsemékers et al. (2026) included for comparison. As the comet receded from  $r_h \sim 1.8$  to  $\sim 3.3$  au,  $Q_{\text{CN}}$  decreased. A weighted power-law fit ( $Q \propto r_h^{-n}$ ) yields an index of  $n = 3.8 \pm 0.1$ , significantly shallower than the inbound slope of  $n = 6.7 \pm 0.1$ . Our derived trend is well-supported by several independent measurements, including TRAPPIST results at similar  $r_h$  (E. Jehin et al. 2025a,b) and the earliest post-perihelion observations at  $r_h = 1.509$  au reported by W. B. Hoogendam et al. (2026).

A similar perihelion asymmetry was observed in the water production rate ( $Q_{\text{H}_2\text{O}}$ ) of 3I, which transitioned from a steep inbound slope ( $n = 5.9 \pm 0.8$ ) to a significantly shallower outbound decline ( $n = 3.3 \pm 0.3$ ; H. Tan et al. 2026). The comparable slopes of  $Q_{\text{H}_2\text{O}}$  and  $Q_{\text{HCN}}$  indicate a relatively stable  $Q_{\text{CN}}/Q_{\text{H}_2\text{O}}$  mixing ratio across perihelion. Specifically, combining our measurements with the  $Q_{\text{H}_2\text{O}}$  data from H. Tan et al. (2026) yields  $Q_{\text{CN}}/Q_{\text{H}_2\text{O}} = 0.23\%–0.17\%$  over  $r_h \sim 1.8–$

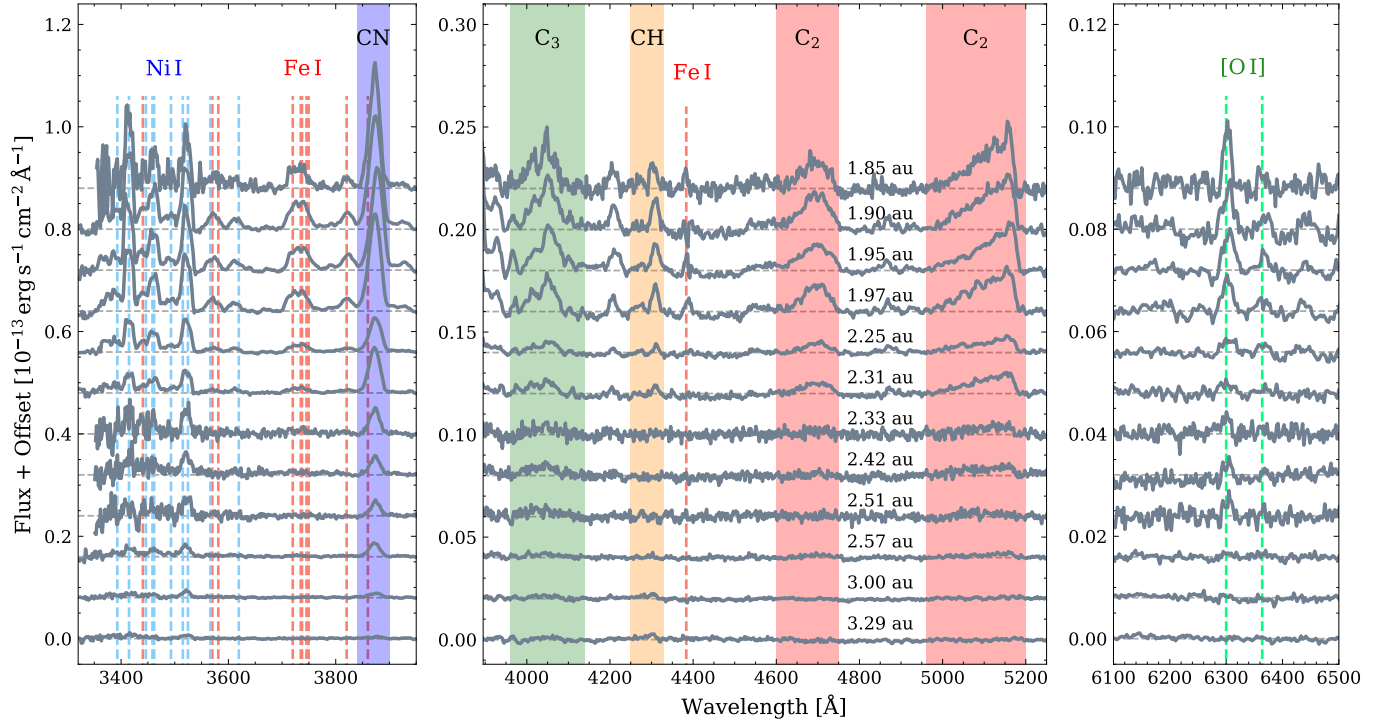


**Figure 1.** Emission spectra of 3I/ATLAS taken with BFOSC and YFOSC. For clarity, the full spectral range is divided into three panels with different vertical offsets to emphasize specific features. The left panel highlights emission lines of Ni I (blue dashed lines) and Fe I (red dashed lines), and the CN violet band (blue shaded). The middle panel shows molecular bands of C<sub>3</sub> (green shaded), CH (orange shaded), and C<sub>2</sub> (red shaded), and lists the heliocentric distance for each spectrum. The right panel displays the [O I]  $\lambda\lambda$ 6300, 6364 doublet (green dashed lines).

3.3 au, in excellent agreement with the inbound value of  $Q_{\text{HCN}}/Q_{\text{H}_2\text{O}} = 0.20 \pm 0.08\%$  reported by *I. M. Coulson et al. (2026)* at 2.1 au.

A stable mixing ratio, however, does not necessarily imply identical outgassing regions or release mechanisms. During the inbound leg,  $Q_{\text{H}_2\text{O}}$  included substantial contributions from icy grains in the extended coma (*B. Yang et al. 2025; Z. Xing et al. 2025; M. A. Cordiner et al. 2025; D. Hutsemékers et al. 2026; H. Tan et al. 2026*), whereas ALMA mapping showed that HCN production was consistent with direct nucleus sublimation (*N. X. Roth et al. 2025*). Similar decoupling between the outgassing regions of H<sub>2</sub>O and CN has also been observed in solar system comets, despite relatively stable mixing ratios (*M. M. Knight & D. G. Schleicher 2013; C. Opitom et al. 2015; K. Villa et al. 2024*). After perihelion, the gradual decline of  $Q_{\text{H}_2\text{O}}$  was attributed to a nearly constant effective active area regulated by decreasing solar insolation (*H. Tan et al. 2026*), yet the spatial origin of our observed CN remains unconstrained.

The mixing ratios of C<sub>3</sub>, C<sub>2</sub>, and CH relative to CN remain generally stable, with no statistically significant trend detected over the observed heliocentric range. The weighted averages yield  $\log(Q_{\text{C}_3}/Q_{\text{CN}}) = -1.06$ ,  $\log(Q_{\text{C}_2}/Q_{\text{CN}}) = -0.13$ , and  $\log(Q_{\text{CH}}/Q_{\text{CN}}) = 0.23$ , in-

dicating moderate depletion in carbon-chain species yet a “typical” CH abundance under the compositional classification of *A. L. Cochran et al. (2012)*.

3I was found to be strongly carbon-chain depleted during the inbound leg as indicated by the extremely low mixing ratios of  $\log(Q_{\text{C}_3}/Q_{\text{CN}}) = -1.47$  and  $\log(Q_{\text{C}_2}/Q_{\text{CN}}) = -0.86$  (*L. E. Salazar Manzano et al. 2025; M. Lazzarin et al. 2026*). Our results indicate that both C<sub>3</sub> and C<sub>2</sub> are significantly less depleted than in the pre-perihelion phase. More enriched values were reported from TRAPPIST observations (*E. Jehin et al. 2025a,b*), with  $\log(Q_{\text{C}_3}/Q_{\text{CN}}) \sim -0.83$  and  $\log(Q_{\text{C}_2}/Q_{\text{CN}}) \sim 0.05$  at  $r_{\text{h}} = 1.76\text{--}1.98$  au, placing 3I even within the “typical” compositional class.

The reduced degree of C<sub>2</sub> depletion after perihelion suggests a delayed release of its parent species from relatively unprocessed subsurface layer or compositional heterogeneity within the nucleus plus seasonal illumination effects around perihelion. A similar interpretation was proposed by *E. Jehin et al. (2025a)* to explain their TRAPPIST measurements and by *M. Belyakov et al. (2026)* to account for the enriched CH<sub>4</sub> abundance observed after perihelion.

In their thirty-year survey, *A. L. Cochran et al. (2012)* reported a lower ratio of  $\log(Q_{\text{CH}}/Q_{\text{CN}}) = 0.02 \pm 0.26$  for

carbon-chain depleted comets, compared to  $0.25 \pm 0.18$  for the “typical” group. However, the large dispersion and the very small depleted sample (only two with CH measurements) render the difference statistically insignificant. Inspection of individual comets in their sample further shows that comets classified as carbon-chain depleted are not consistently depleted in CH, indicating only a weak correlation between CH abundance and carbon-chain species (A. L. Cochran et al. 2012). Our derived ratio of  $\log(Q_{\text{CH}}/Q_{\text{CN}}) = 0.23$  for 3I lies near

the midpoint of the “typical” group and is in good agreement with the long-period comet average of  $0.27 \pm 0.17$  (A. L. Cochran et al. 2012).

Proposed parents of CH observed in the cometary comae include  $\text{CH}_4$  as a nucleus ice or distributed organic compounds (A. L. Cochran et al. 1997). Recent JWST/MIRI measurements show that 3I is enriched in  $\text{CH}_4$  relative to most solar system comets (M. Belyakov et al. 2026). The absence of a correspondingly elevated CH abundance in our observations therefore disfavors  $\text{CH}_4$  as the dominant parent of CH in 3I.

**Table 2.** Production rates and mixing ratios.

Date (UT)	$r_h$ (au)	$\log Q_{\text{CN}}$ ( $\text{s}^{-1}$ )	$\log(Q_{\text{C}_3}/Q_{\text{CN}})$	$\log(Q_{\text{C}_2}/Q_{\text{CN}})$	$\log(Q_{\text{CH}}/Q_{\text{CN}})$	$\log Q_{\text{NiI}}$ ( $\text{s}^{-1}$ )	$\log Q_{\text{FeI}}$ ( $\text{s}^{-1}$ )	$\log(Q_{\text{NiI}}/Q_{\text{FeI}})$
Dec. 2	1.846	$25.34 \pm 0.06$	$-1.06 \pm 0.07$	$-0.11 \pm 0.06$	$0.16 \pm 0.07$	$24.99 \pm 0.02$	$24.81 \pm 0.02$	$0.18 \pm 0.03$
Dec. 4	1.898	$25.52 \pm 0.02$	$-1.03 \pm 0.03$	$-0.12 \pm 0.03$	$0.21 \pm 0.04$	$24.94 \pm 0.09$	$24.80 \pm 0.09$	$0.14 \pm 0.12$
Dec. 6	1.947	$25.49 \pm 0.02$	$-1.00 \pm 0.03$	$-0.14 \pm 0.03$	$0.21 \pm 0.03$	$24.89 \pm 0.09$	$24.76 \pm 0.09$	$0.13 \pm 0.12$
Dec. 7	1.973	$25.50 \pm 0.02$	$-1.06 \pm 0.03$	$-0.12 \pm 0.03$	$0.33 \pm 0.03$	$24.83 \pm 0.09$	$24.68 \pm 0.09$	$0.15 \pm 0.12$
Dec. 17	2.246	$25.29 \pm 0.02$	$-1.15 \pm 0.03$	$-0.15 \pm 0.03$	$0.15 \pm 0.04$	$24.70 \pm 0.09$	$24.30 \pm 0.09$	$0.40 \pm 0.12$
Dec. 19	2.306	$25.44 \pm 0.02$	$-1.12 \pm 0.03$	$-0.15 \pm 0.04$	$0.09 \pm 0.08$	$24.56 \pm 0.09$	$24.17 \pm 0.09$	$0.39 \pm 0.12$
Dec. 20	2.333	$25.16 \pm 0.06$	$-0.94 \pm 0.07$	$-0.17 \pm 0.06$	—	$24.68 \pm 0.02$	$24.17 \pm 0.03$	$0.50 \pm 0.04$
Dec. 23	2.423	$25.10 \pm 0.06$	$-0.91 \pm 0.07$	$0.01 \pm 0.06$	—	$24.60 \pm 0.02$	$23.92 \pm 0.03$	$0.68 \pm 0.04$
Dec. 26	2.509	$24.95 \pm 0.06$	—	—	—	$24.53 \pm 0.02$	—	—
Dec. 28	2.570	$24.95 \pm 0.02$	—	—	—	$24.46 \pm 0.09$	$23.74 \pm 0.09$	$0.72 \pm 0.13$
Jan. 11	3.002	$24.78 \pm 0.03$	—	—	—	$24.29 \pm 0.09$	—	—
Jan. 20	3.293	$24.64 \pm 0.03$	—	—	—	$24.18 \pm 0.09$	—	—

### 3.2. Iron and Nickel

To derive the production rates of FeI and NiI, we employed the three-level atom model of J. Manfroid et al. (2021). Owing to the low spectral resolution, individual lines in our spectra cannot be reliably isolated, precluding the construction of a Boltzmann plot. We therefore adopted a forward-modeling approach and constrained the model parameters within a maximum-likelihood framework.

Using transition data from the NIST Atomic Spectra Database (A. Kramida et al. 2024), we constructed a synthetic spectrum of the form

$$I_{\lambda}^{\text{mod}}(\Theta) = \phi(\lambda) * \left[ \sum_i I_i(\Theta) \delta(\lambda - \lambda'_i) \right], \quad (1)$$

where  $\phi(\lambda)$  represents the Gaussian line profile, and  $*$  denotes convolution.  $I_i(\Theta)$  is the modeled intensity of

the  $i$ -th transition which depends on the excitation temperature ( $T$ ) and column density ( $N$ ). Its detailed formula is given in the supplementary information of J. Manfroid et al. (2021) as Equation (14).

The excitation temperatures of FeI and NiI are affected by the heliocentric radial velocity due to strong absorption lines in the solar spectrum. Given the high heliocentric velocity of 3I, the excitation temperature is expected to be  $T \sim 4500$  K (J. Manfroid et al. 2021). Owing to severe line blending in our spectra, the excitation temperature cannot be independently constrained. We therefore fixed  $T_{\text{FeI}} = 4500$  K<sup>9</sup> and set  $T_{\text{NiI}} = T_{\text{FeI}} + 180$  K = 4680 K for all epochs. The 180 K

<sup>9</sup> The assumption of  $T_{\text{FeI}} = 4500$  K is only  $\sim 100$  K higher than that determined by Boltzmann plot from KCWI data (W. B. Hoogendam et al. 2026), which translates to a difference of only  $\sim 0.1$  dex in the inferred column densities (or production rates).

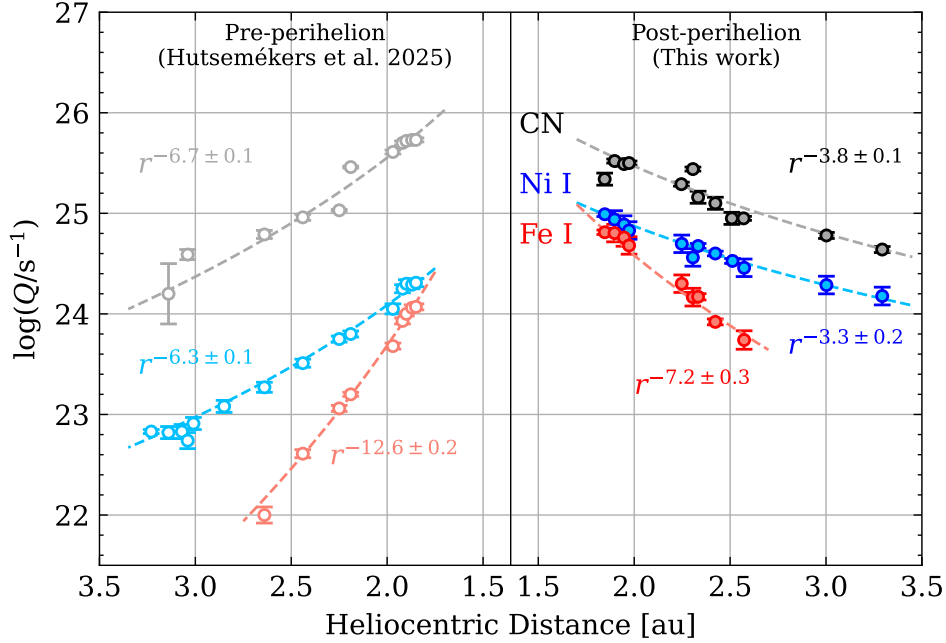


**Figure 2.** Production rates of CN, Ni I, and Fe I as a function of heliocentric distance for 3I/ATLAS. Post-perihelion measurements from this work are shown as filled circles, while pre-perihelion measurements from D. Hutsemékers et al. (2026) are shown as open circles. The species are color-coded as CN—grey, Ni I—blue, and Fe I—red. Dashed lines indicate the corresponding power-law dependencies ( $r_h^{-n}$ ) derived from weighted fits.

is to compensate for a systematic bias in the Ni I/Fe I ratio introduced by the simplified three-level model (see the supplementary information of J. Manfroid et al. (2021) for details).

The laboratory wavelengths  $\lambda_i$  were adjusted using  $\lambda'_i = (1+s) \times \lambda_i - s \times 3650 \text{ \AA}$  to account for residual linear stretch in the wavelength solution blueward of  $3650 \text{ \AA}$  (see Appendix A). The stretch factor  $s$  was treated as a free parameter in the fitting. The free parameter set is thus  $\Theta = \{s, N_{\text{Fe I}}, N_{\text{Ni I}}\}$ .

The synthetic spectrum was fitted to the observed spectrum using Markov Chain Monte Carlo (MCMC) sampling with a Gaussian log-likelihood function,

$$\ln \mathcal{L} = -\frac{1}{2} \sum_{\lambda} \left( \frac{I_{\lambda}^{\text{obs}} - I_{\lambda}^{\text{mod}}}{\sigma_{\lambda}^{\text{obs}}} \right)^2, \quad (2)$$

where  $I_{\lambda}^{\text{obs}}$  and  $\sigma_{\lambda}^{\text{obs}}$  are the observed flux and its uncertainty at  $\lambda$ .

For each epoch, we run the MCMC sampling twice. The first run provides an initial fit to the spectra, from which we adopt the best-fit stretch factor  $s$  to refine the wavelength solution at  $\lambda < 3650 \text{ \AA}$ . We then repeat the flux calibration using the corrected wavelength solution (see Appendix A). The MCMC sampling is subsequently performed on the recalibrated spectra to derive the final column densities  $N_{\text{Fe I}}$  and  $N_{\text{Ni I}}$ , which we convert to production rates ( $Q_{\text{Fe I}}$  and  $Q_{\text{Ni I}}$ ) using Haser’s coma

density model (see J. Manfroid et al. 2021). The resulting  $Q_{\text{Fe I}}$ ,  $Q_{\text{Ni I}}$ , and the  $Q_{\text{Ni I}}/Q_{\text{Fe I}}$  ratio are listed in Table 2 on a logarithmic scale. Due to the high noise level relative to the weakening emission,  $Q_{\text{Fe I}}$  could not be reliably constrained for the epochs of December 26, January 11, and 20.

The logarithmic production rates are shown in Figure 2 as a function of heliocentric distance, with pre-perihelion measurements from D. Hutsemékers et al. (2026) included for comparison. During the inbound leg, Ni I was detected as early as 3.78 au, whereas Fe I was identified only later at 2.64 au (R. Rahatgaonkar et al. 2025; W. B. Hoogendam et al. 2025a,b; D. Hutsemékers et al. 2026). Weighted power-law fits ( $Q \propto r_h^{-n}$ ) to the D. Hutsemékers et al. (2026) measurements yield an inbound index of  $n = 6.3 \pm 0.1$  for Ni I, and a much steeper  $n = 12.6 \pm 0.2$  for Fe I. Such steep heliocentric dependencies and the resulting evolution of the  $Q_{\text{Ni I}}/Q_{\text{Fe I}}$  ratio have been explained as a natural consequence of the temperature-dependent sublimation of the highly volatile metal carbonyls, such as  $\text{Ni}(\text{CO})_4$  and  $\text{Fe}(\text{CO})_5$  (D. Hutsemékers et al. 2026).

In our observations,  $Q_{\text{Fe I}}$  and  $Q_{\text{Ni I}}$  decline as the comet recedes from the Sun. However, weighted power-law fits give outbound indices of  $n = 3.3 \pm 0.2$  and  $n = 7.2 \pm 0.3$  for Ni I and Fe I, respectively, both significantly shallower than the corresponding inbound values. This perihelion asymmetry, analogous to that observed

for  $Q_{\text{H}_2\text{O}}$ , suggests that the release of Fe I and Ni I is likely also regulated by the thermal evolution and progressive surface modification of the nucleus, rather than being controlled solely by the intrinsic volatility of metal carbonyls, which would otherwise produce a more symmetric heliocentric dependence across perihelion.

Moreover, our derived  $Q_{\text{FeI}}$  and  $Q_{\text{NiI}}$  are approximately an order of magnitude higher than those measured at comparable heliocentric distances during the inbound leg (D. Hutsemékers et al. 2026), contrary to the behavior of  $Q_{\text{H}_2\text{O}}$ , which generally remains at a comparable level despite exhibiting asymmetric heliocentric dependencies across perihelion (H. Tan et al. 2026). The contrast indicates that the coma became significantly enriched in metals relative to  $\text{H}_2\text{O}$  in the outbound leg, reinforcing the scenario of subsurface sublimation or seasonal effects on a compositionally heterogeneous nucleus proposed for  $\text{C}_2$ . Our measurements are further supported by W. B. Hoogendam et al. (2026), who derived enriched  $Q_{\text{FeI}} = (9.55 \pm 3.96) \times 10^{25} \text{ s}^{-1}$  and  $Q_{\text{NiI}} = (6.61 \pm 2.74) \times 10^{25} \text{ s}^{-1}$  together with a comparable  $Q_{\text{CN}} = (1.6 \pm 0.5) \times 10^{26} \text{ s}^{-1}$  at 1.509 au.

### 3.3. [O I] $\lambda 6300$ Emission

The [O I]  $\lambda\lambda 6300, 6364$  doublet arises from the electric-dipole forbidden transition from the excited  $^1\text{D}$  state to the  $^3\text{P}$  ground state of atomic oxygen. In cometary comae,  $\text{O}(^1\text{D})$  is primarily produced via the photodissociation of  $\text{H}_2\text{O}$ ,  $\text{CO}_2$ , and  $\text{CO}$ , and has been widely used to infer the production rates of these parent volatiles (e.g., M. Festou & P. D. Feldman 1981; J. P. Morgenthaler et al. 2007; A. J. McKay et al. 2012; A. Decock et al. 2013; M. G. Hyland et al. 2019; C. Opitom et al. 2021).

During the inbound leg, the  $Q_{\text{H}_2\text{O}}$  of 3I increased rapidly but likely remained insufficient for detectable [O I] emission before the comet became unobservable due to its small solar elongation, causing the non-detection of the [O I]  $\lambda\lambda 6300, 6364$  doublet in any inbound spectra despite the extremely high  $\text{CO}_2$  abundance ( $Q_{\text{CO}_2}/Q_{\text{H}_2\text{O}} = 7.6 \pm 0.3$ ; M. A. Cordiner et al. 2025). Our post perihelion spectra, however, were obtained at smaller heliocentric distances, where  $Q_{\text{H}_2\text{O}}$  was higher (H. Tan et al. 2026), and the high  $\text{CO}_2$  abundance was found to persist ( $Q_{\text{CO}_2}/Q_{\text{H}_2\text{O}} \sim 3\text{--}7$ ; M. Belyakov et al. 2026). Therefore, the detection of the [O I]  $\lambda\lambda 6300, 6364$  doublet during the outbound leg is not unexpected.

Whether CO contributes significantly to the observed [O I] emission remains an important question, as its heliocentric behavior can differ from that of  $\text{H}_2\text{O}$  and  $\text{CO}_2$  (O. Harrington Pinto et al. 2022), and it is a key constituent of the metal carbonyls potentially responsible

for the observed tenfold increase in Fe I and Ni I. Pre-perihelion measurements suggest a moderate CO abundance at  $Q_{\text{CO}}/Q_{\text{H}_2\text{O}} = 1.65 \pm 0.09$  (M. A. Cordiner et al. 2025; O. Harrington Pinto et al. 2022). Here we present a simple estimate of  $Q_{\text{CO}}$  based on the residual [O I]  $\lambda 6300$  intensity after subtracting the modeled contributions from  $\text{H}_2\text{O}$  and  $\text{CO}_2$ . The [O I]  $\lambda 6364$  component is excluded from the subsequent analysis owing to its low SNR.

Following A. J. McKay et al. (2012), we relate the wavelength-integrated [O I]  $\lambda 6300$  line intensity  $I_{6300}$  to the column density of a given parent molecule through

$$N = \frac{4\pi \times I_{6300}}{h\nu \times W}, \quad (3)$$

where  $h\nu$  is the photon energy at 6300 Å and  $W$  is the “excitation” rate defined by A. J. McKay et al. (2012). The column density  $N$  is then related to the production rate  $Q$  by Haser’s coma density model (L. Haser 1957).

We estimate the contributions of  $\text{H}_2\text{O}$  and  $\text{CO}_2$  to the [O I]  $\lambda 6300$  emission for the first four observations (December 2–7) by adopting  $Q_{\text{H}_2\text{O}}$  from nearby dates (H. Tan et al. 2026) and extrapolating the two  $Q_{\text{CO}_2}$  measurements from M. Belyakov et al. (2026). Together, these two species account for only 40%–60% of the observed intensity, leaving a substantial residual. If the full residual is attributed to CO, the implied average production rate would be  $Q_{\text{CO}} \gtrsim 1 \times 10^{29} \text{ s}^{-1}$ , corresponding to  $Q_{\text{CO}}/Q_{\text{H}_2\text{O}} \gtrsim 7.5$  at  $r_h \sim 1.9$  au. Both values should be regarded as approximate lower limits, since the large-aperture SOHO/SWAN measurements of  $Q_{\text{H}_2\text{O}}$  included extended coma contributions that produce [O I] emission beyond our slit aperture. Additional uncertainty comes from the extrapolated  $\text{CO}_2$  contribution, which is based on only two measurements, and from the possibility that the residual [O I] emission is not due exclusively to CO, making the inferred  $Q_{\text{CO}}$  only a rough estimate. Nevertheless, if future direct CO measurements from facilities such as JWST/NIRSpec, ALMA, or JCMT confirm the elevated outbound CO abundance inferred here, this would suggest that CO did not track the evolution of  $\text{H}_2\text{O}$  or  $\text{CO}_2$  during this period. The potentially elevated CO abundance may also indicate a simultaneous increase in the production rates of CO and gaseous metals. The implications of this result are discussed in §4.

## 4. DISCUSSION

A statistically significant correlation between  $\log(Q_{\text{C}_2}/Q_{\text{CN}})$  and  $\log(Q_{\text{NiI}}/Q_{\text{FeI}})$  was reported by D. Hutsemékers et al. (2021) across both solar system comets and 2I/Borisov (see Figure 3a), from

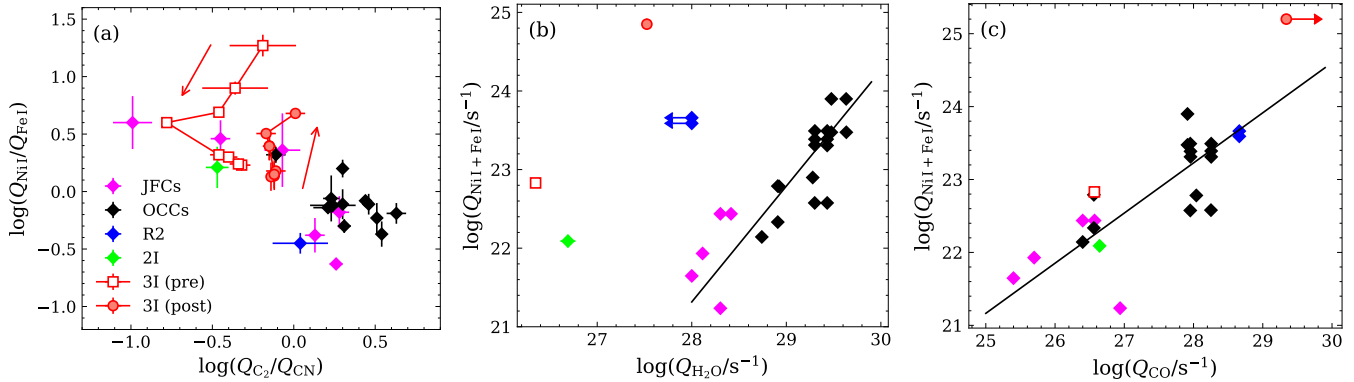


**Figure 3.** Correlations. (a):  $\log(Q_{\text{NiI}}/Q_{\text{FeI}})$  versus  $\log(Q_{\text{C}_2}/Q_{\text{CN}})$ ; (b):  $\log(Q_{\text{NiI}+\text{FeI}})$  versus  $\log(Q_{\text{H}_2\text{O}})$ ; (c):  $\log(Q_{\text{NiI}+\text{FeI}})$  versus  $\log(Q_{\text{CO}})$ . The red arrows in panel (a) indicate the temporal evolution of 3I. The black lines in panel (b) and (c) denote the best-fit correlations with  $Q_{\text{H}_2\text{O}}$  (including all solar system comets except C/2016 R2) and with  $Q_{\text{CO}}$  (including all comets). Post-perihelion measurements of 3I (red circles) are from this work, except for  $Q_{\text{H}_2\text{O}}$ , which is adopted from H. Tan et al. (2026). Pre-perihelion measurements of 3I (open squares) are taken from D. Hutsemékers et al. (2026) and M. A. Cordiner et al. (2025). Comparison data are from D. Hutsemékers et al. (2021), J. Manfroid et al. (2021), and C. Opitom et al. (2021), with colors and marker styles following J. Manfroid et al. (2021) for consistency.

which it was inferred that, similar to  $\log(Q_{\text{C}_2}/Q_{\text{CN}})$ ,  $\log(Q_{\text{NiI}}/Q_{\text{FeI}})$  is also somehow linked to primordial formation conditions (D. Hutsemékers et al. 2021). However, complexity arises when the inbound measurements of 3I from D. Hutsemékers et al. (2026) and outbound measurements from this work are added to the figure. While most comets in the original sample were observed only once or over a narrow range of  $r_h$  and thus appear as static points, repeated observations of 3I span a broader range of  $r_h$  and reveal a displacement across the correlation trend. This behavior raises the question of how to define a representative value of  $\log(Q_{\text{NiI}}/Q_{\text{FeI}})$  for individual objects.

D. Hutsemékers et al. (2026) noted that  $\log(Q_{\text{NiI}}/Q_{\text{FeI}})$  approaches a stable value of  $\sim 0.3$  at  $r_h \lesssim 2$  au, which fits the correlation well. Using the same criterion, our first four measurements yield  $\log(Q_{\text{NiI}}/Q_{\text{FeI}}) \sim 0.2$ . Combined with the less depleted  $\log(Q_{\text{C}_2}/Q_{\text{CN}})$ , this representative value also follows the same correlation. However, W. B. Hoogendam et al. (2026) reported a much lower  $\log(Q_{\text{NiI}}/Q_{\text{FeI}}) = -0.16 \pm 0.03$  at  $r_h = 1.509$  au, suggesting that the relative enhancement of  $Q_{\text{FeI}}$  persists well within  $r_h \lesssim 2$  au. Additional measurements at  $r_h \lesssim 2$  au will be helpful to confirm whether a truly stable  $\log(Q_{\text{NiI}}/Q_{\text{FeI}})$  is reached.

On the other hand, any comprehensive interpretation of the production rates and relative abundances of FeI and NiI requires knowledge of the physical properties of their parent carriers. Detection of FeI and NiI far from the sun indicate the existence of volatile metal-bearing compounds in the nucleus, as refractory dust grains cannot sublimate at the low temperatures characteristic of

these distance (J. Manfroid et al. 2021). This is further supported by the observation that, in solar system comets,  $\log(Q_{\text{NiI}}/Q_{\text{FeI}})$  measured far from the sun are significantly higher than the bulk values inferred from Sun-grazing comets, which exhibit solar abundance (J. Manfroid et al. 2021; D. Hutsemékers et al. 2021).

One leading hypothesis for the volatile parents is metal carbonyls, initially proposed by J. Manfroid et al. (2021) based on a stronger correlation of the metal production rates with CO than with  $\text{H}_2\text{O}$  (see Figure 3b and 3c). This distinction is most clearly illustrated by the chemically peculiar comet C/2016 R2 (PanSTARRS), which, despite being remarkably water-poor, shows simultaneously high production rates of CO and of gaseous FeI and NiI. Similar behavior is also observed in the water-poor interstellar comet 2I/Borisov (C. Opitom et al. 2021).

If the high CO abundance inferred in §3.3 is approximately correct, it would imply a simultaneous enrichment of both CO and the metals by nearly an order of magnitude relative to  $\text{H}_2\text{O}$  compared to the pre-perihelion values, and may therefore offer an additional point of comparison for this picture. As shown in Figure 3b and 3c, while the pre-perihelion measurements (from D. Hutsemékers et al. (2026) and M. A. Cordiner et al. (2025)) and our enriched post-perihelion data both deviate significantly from the  $\text{H}_2\text{O}$  correlation, they remain broadly consistent with the CO trend, tentatively suggesting that the metals are linked to a CO-bearing volatile reservoir, potentially in the form of metal carbonyls.

O. Harrington Pinto et al. (2022) reported that, in solar system comets,  $Q_{\text{CO}}/Q_{\text{H}_2\text{O}}$  shows a more scat-

tered trend with  $r_h$  and an abrupt change in slope near  $\sim 2.5$  au, in contrast to the tighter and more consistent trend followed by  $Q_{\text{CO}_2}/Q_{\text{H}_2\text{O}}$ . They also reported that dynamically new comets tend to display lower  $Q_{\text{CO}}/Q_{\text{CO}_2}$  ratios than returning comets, indicating a depletion of highly volatile CO in the nucleus's surface layers, with deeper CO ices only becoming exposed after gradual thermal erosion during successive perihelion passages (O. Harrington Pinto et al. 2022). The potential enrichment of CO relative to  $\text{CO}_2$  and  $\text{H}_2\text{O}$  inferred for 3I suggest that similar decoupling may also occur in interstellar objects and, if true, the post-perihelion  $Q_{\text{CO}}/Q_{\text{H}_2\text{O}}$  ratio may be more reflective of the nucleus's intrinsic CO abundance than the pre-perihelion value.

Primordial ice stratification offers one natural interpretation for such decoupling. Infrared observations of young stellar objects indicate that CO predominantly freezes out as pure, apolar ice at low temperatures ( $\sim 20$  K), whereas  $\text{CO}_2$  typically co-condenses within polar,  $\text{H}_2\text{O}$ -rich ice layers (A. C. A. Boogert et al. 2015). In this scenario, the decoupling observed in solar system comets and potentially in ISOs could reflect a preserved natal heritage, with the relative abundances of CO,  $\text{CO}_2$ , and  $\text{H}_2\text{O}$  potentially retaining information about the physical conditions and chemical inventory of their parent environments.

## 5. SUMMARY

The main findings of this work are summarized as follows:

1. The post-perihelion production rate of CN declines with a power-law index of  $n = 3.8 \pm 0.1$ , significantly shallower than the steep pre-perihelion slope of  $n = 6.7 \pm 0.1$ . This asymmetry mirrors the behavior of  $\text{H}_2\text{O}$ , and therefore results in a relatively stable mixing ratio of  $Q_{\text{CN}}/Q_{\text{H}_2\text{O}} \sim 0.2\%$  across the perihelion passage.
2. The mixing ratios of  $\text{C}_3$ ,  $\text{C}_2$ , and CH relative to CN remain generally stable over the observed heliocentric range.  $\text{C}_2$  shows a less depleted value of  $\log(Q_{\text{C}_2}/Q_{\text{CN}}) = -0.13$  compared to pre-perihelion, suggesting either delayed release from relatively unprocessed subsurface layers or compositional heterogeneity influenced by seasonal illumination.
3. The outbound production rates of Fe I and Ni I are approximately an order of magnitude higher than those observed at comparable heliocentric distances during the inbound leg. Their asymmetric heliocentric behavior suggests that metal

release is not solely driven by the intrinsic volatility of the parent species, but also regulated by the progressive thermal evolution and surface modification of the nucleus.

4. The [O I]  $\lambda 6300$  emission shows a substantial residual after subtracting the modeled contributions from  $\text{H}_2\text{O}$  and  $\text{CO}_2$ . Attributing the full residual to CO yields an lower limit of  $Q_{\text{CO}}/Q_{\text{H}_2\text{O}} \gtrsim 7.5$  at  $r_h \sim 1.9$  au outbound. The potentially elevated CO abundance relative to  $\text{CO}_2$  and  $\text{H}_2\text{O}$  may suggest partial decoupling among these species, similar to the behavior observed in solar system comets. The simultaneous enrichment of gaseous metals (Fe I and Ni I) and CO relative to  $\text{H}_2\text{O}$  is compatible with the metal carbonyls hypothesis.

## ACKNOWLEDGMENTS

This work is supported by the National Natural Science Foundation of China (NSFC) through the projects 12588202. X.L.Z and X.Y.F acknowledge Yunnan Fundamental Research Project (Grant No. 202501AS070006). S.W. acknowledge support from the Youth Innovation Promotion Association of the CAS with No. 2023065. We acknowledge the support of the staff of the Xinglong 2.16m telescope. This work was partially supported by National Astronomical Observatories, Chinese Academy of Sciences. We acknowledge the support of the staff of the Lijiang 2.4m telescope. Funding for the telescope has been provided by Chinese Academy of Sciences and the People's Government of Yunnan Province.

## AUTHOR CONTRIBUTIONS

R.N.Z. conducted the BFOSC observations, reduced the BFOSC and YFOSC data, performed the spectral modeling, and drafted substantial portions of the manuscript. X.L.Z. contributed to the YFOSC observations, supervised the graduate student, and reviewed the manuscript. B.Y. contributed to the development of the forward-modeling method used in the Fe I and Ni I analysis and a critical review of the manuscript. X.Y.F. contributed to the YFOSC observations. S.W. and J.F.L. secured funding and reviewed the manuscript. Y.H. reviewed the manuscript.

*Facilities:* Beijing: 2.16m, YAO: 2.4m (YFOSC)

*Software:* astropy (Astropy Collaboration et al. 2013, 2018, 2022), astroquery (A. Ginsburg et al. 2019),

astro-wcipy (R. Zhao 2023), ccdproc (M. W. Craig et al. 2015), emcee (D. Foreman-Mackey et al. 2013), sbpy (M.

Mommert et al. 2019) spectres (A. C. Carnall 2017), specutils (Astropy-Specutils Development Team 2019),

## APPENDIX

### A. DATA REDUCTION

For both BFOSC and YFOSC observations, the data were first reduced with the ASTRO-PLPY<sup>8</sup> package following standard procedures for long-slit spectroscopy. All science exposures were bias-subtracted, flat-field corrected, and cleaned of cosmic rays using either median combination or the L.A.Cosmic algorithm (P. G. van Dokkum 2001). Geometric distortion in the spatial direction was characterized and corrected by fitting the curved arc lines with B-spline functions. Wavelength and flux calibrations were then performed to produce fully reduced two-dimensional spectra. One-dimensional spectra were extracted using a fixed aperture of 80 pixels, corresponding to 21''9 for BFOSC and 22''6 for YFOSC.

The flux calibration for the YFOSC observations required additional considerations. Owing to scheduling constraints, 3I and the flux standard Feige 56 were observed at noticeably different airmasses on several December nights (see Table 3). On the other hand, the solar analog BD+00 2717 on those epochs was observed at airmasses better matched to that of 3I. To minimize differential atmospheric effects and to ensure internal consistency among epochs, we therefore adopted BD+00 2717 as the flux calibrator for all December observations. By convolving the flux-calibrated spectra of BD+00 2717 with photometric filters and comparing the resulting synthetic magnitudes with catalog values, we determined that the December 7 spectrum exhibited the most reliable absolute flux level and color slope. It was consequently adopted as a reference, and spectra from the other epochs were scaled relative to it to achieve consistent flux normalization across epochs. For the two January observations, a different solar analog was observed owing to the rapid apparent motion of 3I on the sky, and the calibration in those cases followed standard procedures.

During the subsequent spectral analysis, we found that the wavelength accuracy in the blue region is limited by the available reference lines. For BFOSC, the Fe-Ar arc lamp provides lines down to  $\sim 3500 \text{ \AA}$ , whereas for YFOSC the planetary nebula NGC 2392 offers lines only to  $\sim 3700 \text{ \AA}$ , leaving significant residual deviations at blue end. Typical deviations reach  $\sim 7 \text{ \AA}$  at  $3300 \text{ \AA}$  for BFOSC and  $\sim 25 \text{ \AA}$  for YFOSC. This directly affects the analysis of Fe I and Ni I emission features. To account for this, a simple linear stretch correction was incorporated into the spectral modeling (see §3.2). After applying the derived stretch correction to the wavelength solution, we repeated the flux calibration to obtain a more accurate absolute flux scale.

**Table 3.** Full observation log of 3I/ATLAS.

Date of 2025 (UT)	Object	$\Delta^a$ (au)	$r_h^b$ (au)	$\dot{r}_h^c$ (km s <sup>-1</sup> )	$\alpha^d$ (°)	Tel./Inst.	$\lambda^e$ (nm)	Slit Width (")	Exposure (s)	Airmass
Dec. 2	3I/ATLAS	1.892	1.846	42.44	30.5	2.16-m/BFOSC	330–660	2.3	4×300	1.72–1.61
	HR 4468					...	...	...	2	1.71
	HD 107072					...	...	...	180	1.74
Dec. 4	Hilt 102					2.40-m/YFOSC	320–930	2.5	180	1.25
	BD+00 2717					...	...	...	60	1.37
	3I/ATLAS	1.872	1.898	43.71	30.3	...	...	...	300	1.21
Dec. 6	3I/ATLAS	1.855	1.947	44.78	29.9	2.40-m/YFOSC	320–930	2.5	4×300	1.78–1.60
	BD+00 2717					...	...	...	60	1.36
	Feige 56					...	...	...	90	1.53
Dec. 7	3I/ATLAS	1.846	1.973	45.32	29.6	2.40-m/YFOSC	320–930	2.5	3×300	1.47–1.40
	BD+00 2717					...	...	...	60	1.27

**Table 3** *continued*

**Table 3** (*continued*)

Date of 2025 (UT)	Object	$\Delta^a$ (au)	$r_h^b$ (au)	$\dot{r}_h^c$ (km s <sup>-1</sup> )	$\alpha^d$ (°)	Tel./Inst.	$\lambda^e$ (nm)	Slit Width (")	Exposure (s)	Airmass
	Feige 56					...	...	...	90	1.38
Dec. 17	3I/ATLAS	1.798	2.246	49.48	25.2	2.40-m/YFOSC	320–930	2.5	2×300	1.45–1.41
	BD+00 2717					...	...	...	60	1.50
	Feige 56					...	...	...	90	1.79
Dec. 19	3I/ATLAS	1.798	2.306	50.15	23.9	2.40-m/YFOSC	320–930	2.5	2×300	1.07
	NGC 2392					...	...	...	60	1.30
	BD+00 2717					...	...	...	60	1.13
	Feige 56					...	...	...	90	1.12
Dec. 20	3I/ATLAS	1.799	2.333	50.43	23.3	2.16-m/BFOSC	330–660	2.3	3×300	1.22–1.21
	TYC 274-696-1					...	...	...	180	1.35
	Feige 56					...	...	...	600	1.26
Dec. 23	3I/ATLAS	1.807	2.423	51.28	21.1	2.16-m/BFOSC	330–660	2.3	8×300	1.18–1.22
	TYC 274-696-1					...	...	...	3×180	1.26
	Feige 56					...	...	...	600	1.14
Dec. 26	3I/ATLAS	1.823	2.509	52.00	19.0	2.16-m/bFOSC	330–660	2.3	8×300	1.19–1.26
	TYC 274-696-1					...	...	...	3×180	1.25–1.26
	Feige 56					...	...	...	600	1.14
Dec. 28	3I/ATLAS	1.840	2.570	52.45	17.4	2.40-m/YFOSC	320–930	2.5	300	1.13
	NGC 2392					...	...	...	60	1.04
	BD+00 2717					...	...	...	60	1.34
	Feige 56					...	...	...	90	1.51
Jan. 11 <sup>f</sup>	3I/ATLAS	2.064	3.002	54.76	6.8	2.40-m/YFOSC	320–930	2.5	2×300	1.13–1.11
	NGC 2392					...	...	...	60	1.01
	HR 3454					...	...	...	2	1.15
	HD 89010					...	...	...	6	1.26
Jan. 20 <sup>f</sup>	3I/ATLAS	2.311	3.293	55.75	1.2	2.40-m/YFOSC	320–930	2.5	600	1.27
	HD 89010					...	...	...	5	1.02
	GD108					...	...	...	120	1.28

<sup>a</sup>Geocentric distance.<sup>b</sup>Heliocentric distance.<sup>c</sup>Heliocentric radial velocity.<sup>d</sup>Phase angle.<sup>e</sup>Wavelength range.<sup>f</sup>Date of 2026.

## REFERENCES

Astropy Collaboration, Robitaille, T. P., Tollerud, E. J.,  
et al. 2013, *A&A*, 558, A33,  
doi: 10.1051/0004-6361/201322068

Astropy Collaboration, Price-Whelan, A. M., Sipőcz, B. M.,  
et al. 2018, *AJ*, 156, 123, doi: 10.3847/1538-3881/aabc4f

- Astropy Collaboration, Price-Whelan, A. M., Lim, P. L., et al. 2022, *ApJ*, 935, 167, doi: [10.3847/1538-4357/ac7c74](https://doi.org/10.3847/1538-4357/ac7c74)
- Astropy-Specutils Development Team. 2019, *Specutils*: Spectroscopic analysis and reduction, Astrophysics Source Code Library, record ascl:1902.012 <http://ascl.net/1902.012>
- Bagnulo, S., Cellino, A., Kolokolova, L., et al. 2021, *Nature Communications*, 12, 1797, doi: [10.1038/s41467-021-22000-x](https://doi.org/10.1038/s41467-021-22000-x)
- Belyakov, M., Wong, I., Bolin, B. T., et al. 2026, *arXiv e-prints*, arXiv:2601.22034, doi: [10.48550/arXiv.2601.22034](https://doi.org/10.48550/arXiv.2601.22034)
- Bodewits, D., Noonan, J. W., Feldman, P. D., et al. 2020, *Nature Astronomy*, 4, 867, doi: [10.1038/s41550-020-1095-2](https://doi.org/10.1038/s41550-020-1095-2)
- Boogert, A. C. A., Gerakines, P. A., & Whittet, D. C. B. 2015, *ARA&A*, 53, 541, doi: [10.1146/annurev-astro-082214-122348](https://doi.org/10.1146/annurev-astro-082214-122348)
- Borisov, G., Birtwhistle, P., Bacci, P., et al. 2019, *Central Bureau Electronic Telegrams*, 4666, 1
- Carnall, A. C. 2017, *arXiv e-prints*, arXiv:1705.05165, doi: [10.48550/arXiv.1705.05165](https://doi.org/10.48550/arXiv.1705.05165)
- Cochran, A. L., Barker, E. S., & Gray, C. L. 2012, *Icarus*, 218, 144, doi: [10.1016/j.icarus.2011.12.010](https://doi.org/10.1016/j.icarus.2011.12.010)
- Cochran, A. L., Boice, D. C., Barker, E. S., & Laffont, C. 1997, *Earth Moon and Planets*, 78, 85, doi: [10.1023/A:1006235715217](https://doi.org/10.1023/A:1006235715217)
- Cordiner, M. A., Milam, S. N., Biver, N., et al. 2020, *Nature Astronomy*, 4, 861, doi: [10.1038/s41550-020-1087-2](https://doi.org/10.1038/s41550-020-1087-2)
- Cordiner, M. A., Roth, N. X., Kelley, M. S. P., et al. 2025, *ApJL*, 991, L43, doi: [10.3847/2041-8213/ae0647](https://doi.org/10.3847/2041-8213/ae0647)
- Coulson, I. M., Kuan, Y.-J., Charnley, S. B., et al. 2026, *MNRAS*, 546, stag063, doi: [10.1093/mnras/stag063](https://doi.org/10.1093/mnras/stag063)
- Craig, M. W., Crawford, S. M., Deil, C., et al. 2015, *ccdproc*: CCD data reduction software, Astrophysics Source Code Library, record ascl:1510.007 <http://ascl.net/1510.007>
- Decock, A., Jehin, E., Hutsemékers, D., & Manfroid, J. 2013, *A&A*, 555, A34, doi: [10.1051/0004-6361/201220414](https://doi.org/10.1051/0004-6361/201220414)
- Denneau, L., Siverd, R., Tonry, J., et al. 2025, *Minor Planet Electronic Circulars*, 2025-N12, doi: [10.48377/MPEC/2025-N12](https://doi.org/10.48377/MPEC/2025-N12)
- Fan, Z., Wang, H., Jiang, X., et al. 2016, *PASP*, 128, 115005, doi: [10.1088/1538-3873/128/969/115005](https://doi.org/10.1088/1538-3873/128/969/115005)
- Festou, M., & Feldman, P. D. 1981, *A&A*, 103, 154
- Fitzsimmons, A., Meech, K., Matrà, L., & Pfalzner, S. 2024, in *Comets III*, ed. K. J. Meech, M. R. Combi, D. Bockelée-Morvan, S. N. Raymond, & M. E. Zolensky, 731–766, doi: [10.2458/azu\\_uapress.9780816553631-ch022](https://doi.org/10.2458/azu_uapress.9780816553631-ch022)
- Fitzsimmons, A., Snodgrass, C., Rozitis, B., et al. 2018, *Nature Astronomy*, 2, 133, doi: [10.1038/s41550-017-0361-4](https://doi.org/10.1038/s41550-017-0361-4)
- Foreman-Mackey, D., Hogg, D. W., Lang, D., & Goodman, J. 2013, *PASP*, 125, 306, doi: [10.1086/670067](https://doi.org/10.1086/670067)
- Ginsburg, A., Sipőcz, B. M., Brasseur, C. E., et al. 2019, *AJ*, 157, 98, doi: [10.3847/1538-3881/aafc33](https://doi.org/10.3847/1538-3881/aafc33)
- Harrington Pinto, O., Womack, M., Fernandez, Y., & Bauer, J. 2022, *PSJ*, 3, 247, doi: [10.3847/PSJ/ac960d](https://doi.org/10.3847/PSJ/ac960d)
- Haser, L. 1957, *Bulletin de la Societe Royale des Sciences de Liege*, 43, 740
- Hoogendam, W. B., Shappee, B. J., Wray, J. J., et al. 2025a, *arXiv e-prints*, arXiv:2510.11779, doi: [10.48550/arXiv.2510.11779](https://doi.org/10.48550/arXiv.2510.11779)
- Hoogendam, W. B., Kuesters, D., Shappee, B. J., et al. 2025b, *arXiv e-prints*, arXiv:2512.09020, doi: [10.48550/arXiv.2512.09020](https://doi.org/10.48550/arXiv.2512.09020)
- Hoogendam, W. B., Jones, D. O., Yang, B., et al. 2026, *arXiv e-prints*, arXiv:2601.16983, doi: [10.48550/arXiv.2601.16983](https://doi.org/10.48550/arXiv.2601.16983)
- Hutsemékers, D., Manfroid, J., Jehin, E., Opatom, C., & Moulane, Y. 2021, *A&A*, 652, L1, doi: [10.1051/0004-6361/202141554](https://doi.org/10.1051/0004-6361/202141554)
- Hutsemékers, D., Manfroid, J., Jehin, E., et al. 2026, *A&A*, 706, A43, doi: [10.1051/0004-6361/202557484](https://doi.org/10.1051/0004-6361/202557484)
- Hyland, M. G., Fitzsimmons, A., & Snodgrass, C. 2019, *MNRAS*, 484, 1347, doi: [10.1093/mnras/stz075](https://doi.org/10.1093/mnras/stz075)
- Jehin, E., Hmiddouch, S., Aravind, K., et al. 2025a, *The Astronomer's Telegram*, 17515, 1
- Jehin, E., Hmiddouch, S., Aravind, K., et al. 2025b, *The Astronomer's Telegram*, 17538, 1
- Jewitt, D., & Seligman, D. Z. 2023, *ARA&A*, 61, 197, doi: [10.1146/annurev-astro-071221-054221](https://doi.org/10.1146/annurev-astro-071221-054221)
- Knight, M. M., & Schleicher, D. G. 2013, *Icarus*, 222, 691, doi: [10.1016/j.icarus.2012.06.004](https://doi.org/10.1016/j.icarus.2012.06.004)
- Kramida, A., Ralchenko, Y., Reader, J., & NIST ASD Team. 2024, *NIST Atomic Spectra Database (ver. 5.12)*, doi: [10.18434/T4W30F](https://doi.org/10.18434/T4W30F)
- Lazzarin, M., Mura, A. C., La Forgia, F., et al. 2026, *ApJL*, 998, L30, doi: [10.3847/2041-8213/ae3dd7](https://doi.org/10.3847/2041-8213/ae3dd7)
- Lisse, C., Rustamkulov, Z., Bach, Y., et al. 2026, in *American Astronomical Society Meeting Abstracts*, Vol. 58, American Astronomical Society Meeting Abstracts, 251.02
- Manfroid, J., Hutsemékers, D., & Jehin, E. 2021, *Nature*, 593, 372, doi: [10.1038/s41586-021-03435-0](https://doi.org/10.1038/s41586-021-03435-0)
- McKay, A. J., Chanover, N. J., Morgenthaler, J. P., et al. 2012, *Icarus*, 220, 277, doi: [10.1016/j.icarus.2012.04.030](https://doi.org/10.1016/j.icarus.2012.04.030)
- Meech, K. J., Weryk, R., Micheli, M., et al. 2017, *Nature*, 552, 378, doi: [10.1038/nature25020](https://doi.org/10.1038/nature25020)

- Micheli, M., Farnocchia, D., Meech, K. J., et al. 2018, *Nature*, 559, 223, doi: [10.1038/s41586-018-0254-4](https://doi.org/10.1038/s41586-018-0254-4)
- Mommert, M., Kelley, M., de Val-Borro, M., et al. 2019, *The Journal of Open Source Software*, 4, 1426, doi: [10.21105/joss.01426](https://doi.org/10.21105/joss.01426)
- Morgenthaler, J. P., Harris, W. M., & Combi, M. R. 2007, *ApJ*, 657, 1162, doi: [10.1086/511062](https://doi.org/10.1086/511062)
- Opitom, C., Jehin, E., Manfroid, J., et al. 2015, *A&A*, 584, A121, doi: [10.1051/0004-6361/201526427](https://doi.org/10.1051/0004-6361/201526427)
- Opitom, C., Jehin, E., Hutsemékers, D., et al. 2021, *A&A*, 650, L19, doi: [10.1051/0004-6361/202141245](https://doi.org/10.1051/0004-6361/202141245)
- Rahatgaonkar, R., Carvajal, J. P., Puzia, T. H., et al. 2025, *ApJL*, 995, L34, doi: [10.3847/2041-8213/ae1cbc](https://doi.org/10.3847/2041-8213/ae1cbc)
- Roth, N. X., Cordiner, M. A., Bockelée-Morvan, D., et al. 2025, arXiv e-prints, arXiv:2511.20845, doi: [10.48550/arXiv.2511.20845](https://doi.org/10.48550/arXiv.2511.20845)
- Salazar Manzano, L. E., Lin, H. W., Taylor, A. G., et al. 2025, *ApJL*, 993, L23, doi: [10.3847/2041-8213/ae1232](https://doi.org/10.3847/2041-8213/ae1232)
- Tan, H., Yan, X., & Li, J.-Y. 2026, *ApJL*, 998, L22, doi: [10.3847/2041-8213/ae3c97](https://doi.org/10.3847/2041-8213/ae3c97)
- van Dokkum, P. G. 2001, *PASP*, 113, 1420, doi: [10.1086/323894](https://doi.org/10.1086/323894)
- Villa, K., Knight, M., Schleicher, D., Skiff, B., & Larsen, J. 2024, in *American Astronomical Society Meeting Abstracts*, Vol. 243, American Astronomical Society Meeting Abstracts #243, 363.05
- Wang, C.-J., Bai, J.-M., Fan, Y.-F., et al. 2019, *Research in Astronomy and Astrophysics*, 19, 149, doi: [10.1088/1674-4527/19/10/149](https://doi.org/10.1088/1674-4527/19/10/149)
- Williams, G. V., Sato, H., Sarneczky, K., et al. 2017, *Central Bureau Electronic Telegrams*, 4450, 1
- Xing, Z., Oset, S., Noonan, J., & Bodewits, D. 2025, *ApJL*, 991, L50, doi: [10.3847/2041-8213/ae08ab](https://doi.org/10.3847/2041-8213/ae08ab)
- Yang, B., Meech, K. J., Connelley, M., Zhao, R., & Keane, J. V. 2025, *ApJL*, 992, L9, doi: [10.3847/2041-8213/ae08a7](https://doi.org/10.3847/2041-8213/ae08a7)
- Ye, Q.-Z., Zhang, Q., Kelley, M. S. P., & Brown, P. G. 2017, *ApJL*, 851, L5, doi: [10.3847/2041-8213/aa9a34](https://doi.org/10.3847/2041-8213/aa9a34)
- Zhang, J., Shapiro, A. I., Bi, S., et al. 2020, *ApJL*, 894, L11, doi: [10.3847/2041-8213/ab8795](https://doi.org/10.3847/2041-8213/ab8795)
- Zhao, R. 2023, wcpy: Wavelength Calibrator., *Astrophysics Source Code Library*, record ascl:2311.001 <http://ascl.net/2311.001>